

Phonon anharmonicity in multi-layered WS₂ explored by first-principles and Raman studies

Konrad Wilczyński^{1}, Arkadiusz P. Gertych¹, Karolina Czerniak-Łosiewicz¹, Jakub Sitek¹, Mariusz Zdrojek¹*

¹ Faculty of Physics, Warsaw University of Technology, Koszykowa 75, 00-662 Warsaw, Poland

*Corresponding author:

Konrad.Wilczynski@pw.edu.pl

This is the accepted version of the authors' submitted manuscript, while the published journal article is available at <https://doi.org/10.1016/j.actamat.2022.118299>.

© 2025. This manuscript version is made available under the CC-BY-NC-ND 4.0 license <https://creativecommons.org/licenses/by-nc-nd/4.0/>.

Abstract

Anharmonicity is an essential property of two-dimensional materials due to its significant impact on lattice dynamics – involving interactions between phonons, thermal expansion of the structure, and interaction with the substrate. The effects manifest in temperature-dependent redshifts of the phonon frequencies and reduced lifetime. In this work, we investigate phonon anharmonicity in supported 1–5 layered WS_2 by performing Raman measurements in the temperature range of 80–500 K and explore the results by ab-initio DFT study. An ab-initio model including three-phonon interaction processes and thermal expansion of all geometrical degrees of freedom (in-plane lattice constant, interlayer distance, and monolayer thickness) well describes the experimental temperature trends of the fundamental E_{2g}^1 (in-plane) and A_{1g} (out-of-plane) phonon modes, giving a great promise of using simulation to quantitatively analyze phonon propagation and heat transport in multi-layered two-dimensional materials. The models predict a noticeable increase in the temperature-induced slope of A_{1g} vibrations' frequency with the number of layers – primarily due to the thermal expansion of interlayer distance. Additionally, we study the impact of the substrate on the phonon properties – concerning cumulated effects of induced strain and electron doping. We show that the effect of biaxial strain is the most significant in the E_{2g}^1 phonon mode and independent of the number of layers, while the excess charge is more significant in thin films and affects mainly the A_{1g} mode. The presented studies based on a combination of ab-initio and experimental approaches can be extended to quantitatively analyze phonon evolution with structural modification and external stimuli.

Keywords: DFT, First-principles calculation, Raman spectroscopy, Thin films, Tungsten disulfide

1. Introduction

Tungsten disulfide (WS_2) [1] (Fig. 1a) belongs to the group of transition-metal dichalcogenides (TMDCs) [2], which crystallizes in layered van der Waals structures. Such crystals, especially in the form of two-dimensional nanometer-thin sheets, attract wide attention due to their enormous variety of favorable physical properties from the point of view of potential applications [3–5]. Specifically, as nanometer-thin WS_2 films provide easily tunable bandgap – e.g., by strain [6], doping [7], and external electric field [8], they are promising as part of electronic and optoelectronic devices like field-effect transistors [9], photodetectors [10], and solar cells [11]. Additionally, physical properties of two-dimensional TMDCs, such as electronic structure, significantly depend on the film thickness [3] – indicating the high importance of this structural property.

Any application of TMDCs in non-zero temperature involves vibrational motion of ions, which can interact with themselves due to phonon anharmonicity [12], and with electrons, by means of electron-phonon coupling [13]. Here, we focus on anharmonicity, which is understood as the presence of any cubic or higher-order terms of the interatomic potential. Anharmonicity occurs in any solid-state, and its typical microscopic sources include lone-pair electrons in the system (leading to interaction asymmetry) [14], metavalent bonding [15], and large-displacement rattling vibrations [16]. The effect causes an amplitude dependence of the phonon frequencies and lifetimes, leading to their temperature evolution and directly affecting phonon-controlled heat transport in the crystal [17]. Additionally, anharmonicity induces the dependence of phonon dispersion on the system's lattice parameters, involving its thermal expansion and affecting all physical properties. Therefore, to quantitatively understand the effect of thermally induced lattice vibrations on the solid state's properties, it is necessary to study the anharmonicity of the interatomic potential and its impact on phonon propagation and interaction properties. The importance

of such research arises not only from the basic research perspective. It is also crucial for spectroscopic characterization of the samples to separate the investigated physical property from temperature-dependent anharmonicity-induced effects. In particular, Raman measurements [18] of the phonons' frequencies and lifetimes are widely used to study such properties as defects formation [19], structural disorder [20], doping [21], strain [22], and the number of layers [23] – provided that the quantitative correlations are known. One must be aware that any investigated physical property can affect harmonic and anharmonic (temperature-dependent) phonon behaviors.

Although a deep understanding of phonon anharmonicity is crucial for controlling heat transport in practical applications and providing a strict interpretation of spectroscopic measurements, the reported studies of anharmonicity in 2D materials are primarily experimental. To date, the temperature dependence of the phonon frequencies in TMDCs has been widely studied with Raman spectroscopy [24], including WS₂ monolayers [25], bilayers [26], few-layered nanosheets [27], thin films [28], and bulk-like thick samples [29,30]. The reported samples were prepared with different methods and supported on a wide choice of substrates or suspended, resulting in different temperature dependences of phonon frequencies [27]. So far, no detailed study has been reported for WS₂ with varying number of layers, but such works exist for MoS₂ [31], MoTe₂ [32], and WSe₂ [33]. However, the experimental studies usually take only phonon energies into account, while the lifetime is also of significant importance. Moreover, the quantitative analysis of phonon anharmonicity is typically performed on the grounds of non-linear regression using compact and approximated formulas like the Balkanski model of phonon-phonon interactions [34] and the Grüneisen model to represent the impact of thermal expansion [33,35]. This approach involves fitting multiple independent parameters to experimental data, leading to significant uncertainties and limited or incorrect conclusions.

The most beneficial approach to analyzing the spectroscopic data is the use of first-principles modeling. Suppose model parameters and the simulated harmonic and anharmonic vibrational properties of the structure had been previously verified on the grounds of a carefully designed experiment. In that case, the spectroscopic measurement combined with an accurate model can provide well-grounded and quantitative information about the structural modification (e.g., defects, disorder, number of layers) and external stimuli (e.g., temperature, pressure, strain, doping) in the sample, by comparing to the measured phonon evolution. Inversely, the simulation can predict the effects of given structural modification or external stimuli on the vibrational properties and phonon-controlled heat transport, indicating the most attractive configurations for the desired application – to be deeper investigated experimentally. The main limitation of the first-principles approach is related to available computational resources, which confines the available systems to periodic supercells with a sufficiently small number of atoms – e.g., only structural disorders with a specific periodicity can be considered. Additionally, one has to be aware of approximations used in the DFT simulation – particularly, the choice of the exchange-correlation functionals and the approach to include van der Waals interactions – requiring the models to be verified by comparison with an experiment. To date, the computational approach has rarely been used to study phonon anharmonicity in 2D materials – the reports include temperature-dependent DFT studies of phonons in single-layer and bilayer MoS₂ [36], black phosphorus [37], and graphene [38]. Other reports used simplified approaches such as quasi-harmonic approximation [39] and molecular dynamics [40], with limited accuracy and range of applicability.

In this work, we study phonon anharmonicity in thin-film WS₂ as a function of one of the most important structural properties of layered material – the number of layers in the film – by performing the

temperature-dependent Raman measurements in the range 80–500 K for exfoliated (Fig. 1b, c) and CVD-grown (see *Supplementary Information*) flakes. We explored the results by comprehensive first-principles DFT simulations of anharmonicity-affected phonon energies and corresponding bandwidths of multi-layered WS_2 , in the temperature range 0–500 K, considering fundamental E_{2g}^1 (in-plane) and A_{1g} (out-of-plane) optical phonon modes. The models covered three-phonon interaction processes and thermal expansion of the lattice: in-plane lattice constant, the separation distance between WS_2 layers, and thickness of the layers. We report thermal expansion of the layer thickness for the first time, to our knowledge. Additionally, we calculated the substrate impact on the phonon harmonic frequencies – concerning mixed effects of strain and charge doping. We obtain good agreement between theory and experiment, which shows a great promise of using the theoretical approach to study harmonic and anharmonic properties of lattice vibrations in multi-layered WS_2 and other 2D materials, as well as to quantitatively analyze their evolution with external stimuli, defects, and structural disorder.

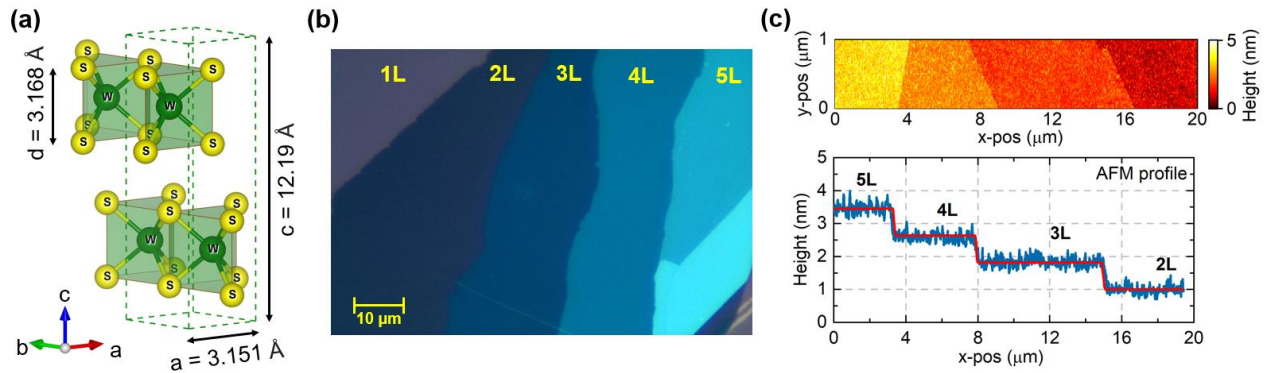


Fig. 1. (a) Structure of the 2H- WS_2 crystal – the geometrical parameters are given based on DFT simulation at the temperature of 300 K. Green dashed lines represent a unit cell of the bulk crystal. (b) Optical microscopy photography of exfoliated WS_2 films with different numbers of layers. (c) Typical AFM picture of terrace flake – here with 2 to 5 layers of WS_2 .

2. Results and discussion

2.1. Evolution of phonons in multi-layered WS_2 – harmonic approximation

Under the harmonic approximation, the movement of ions in any periodic system can be described in terms of independent, vibrational degrees of freedom – phonon modes – with well-defined wavevectors, atomic displacements, and frequencies (energies) [41]. To better understand the phonon structure of monolayer, multi-layered, and bulk 2H- WS_2 crystals, we performed first-principles density functional theory (DFT) simulations (see the section 3). The simulated phonon dispersion and density of states, as presented in Fig. 2a, indicate that the phonon bands of the 1L- WS_2 and bulk WS_2 crystals are similar to each other. However, each phonon branch of the 1L- WS_2 structure splits into two different branches in bulk WS_2 – with opposite vibrations in the adjacent layers [18]. In the case of optical phonons, the most significant frequency shift is observed in the $A_{2u}(\Gamma)$ bulk mode – its frequency is reduced by about 6 cm^{-1} compared to the corresponding monolayer mode. Acoustic phonon branches also split, leading to the formation of low-energy shear E_{2g}^2 and breathing B_{2g}^2 modes at Γ point [42]. In the case of n -layered WS_2 slabs, each phonon mode corresponding to monolayer WS_2 splits into n new modes – they are located between the initial branch of the monolayer and one of the split branches of the bulk.

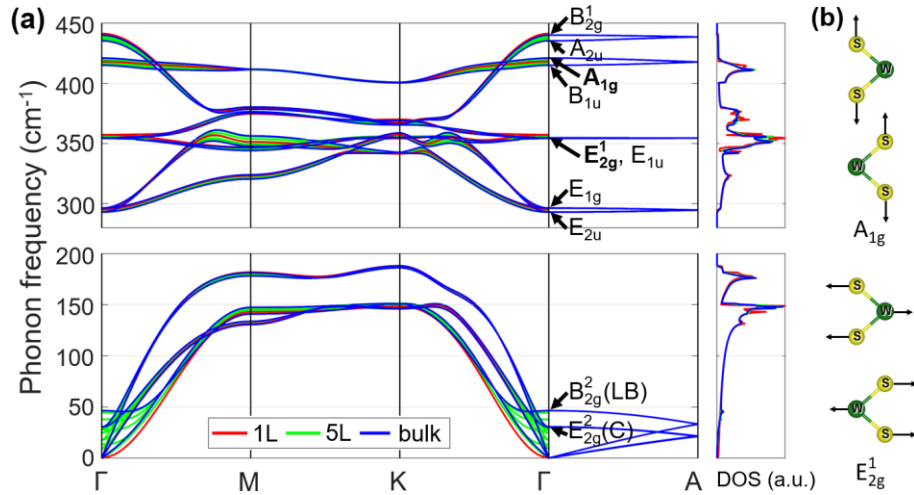


Fig. 2. (a) Calculated phonon dispersion and the corresponding phonon density of states of 1L-WS₂ (red), 5L-WS₂ (green), and bulk WS₂ (blue) in the harmonic approximation; the arrows indicate Γ -point phonon modes of bulk 2H-WS₂. (b) Polarization vectors of the bulk Raman active phonon modes $E_{2g}^1(\Gamma)$ and $A_{1g}(\Gamma)$.

Raman-active optical modes (Fig. 2b), denoted by E_{2g}^1 (in-plane) and A_{1g} (out-of-plane) for bulk 2H-WS₂, are commonly studied experimentally and of the most significant interest in the literature. The E_{1g} and shear E_{2g}^2 modes are also Raman-active, but the former is inactive in backscattering configuration [18], and the latter is less widely studied due to its low energy – below typical Raman spectral ranges. The evolution of the fundamental zone-center E_{2g}^1 and A_{1g} phonon frequencies with different numbers of layers in WS₂ nanosheets is presented in Fig. 3, Tab. S1, and in Fig. S5 in the section 2.2.1 in *Supplementary Information*. We observe the thickness-dependent evolution of the phonon frequencies, which main physical basis has already been reported [43,44]. Interestingly, in multi-layered WS₂, each phonon characteristic for monolayer WS₂ splits into as many phonons as many layers in the film (Fig. S5) – for simplicity, we refer to all “in-plane” and “out-of-plane” Raman-active harmonic phonons as “ E_{2g}^1 ” and “ A_{1g} ”, respectively, following the terminology in bulk crystals. Strikingly, in the case of the in-plane E_{2g}^1 vibrations in WS₂ with three or more layers, there are two slightly separated split Raman-intensive phonon modes – with exterior (surface) or interior (bulk) layers vibrating. Although frequencies of the two split modes barely change with the number of layers, their relative Raman intensities (as given in Fig. 3) evolve. The intensity is transferred from the higher- to lower-frequency mode, and due to a low separation of the split modes (about 1 cm⁻¹), the corresponding Raman bands can be interpreted as a single band with a thickness-dependent mean position. Such splitting of the E_{2g}^1 phonon mode’s Raman intensity has been previously shown using ab-initio simulations [44–46].

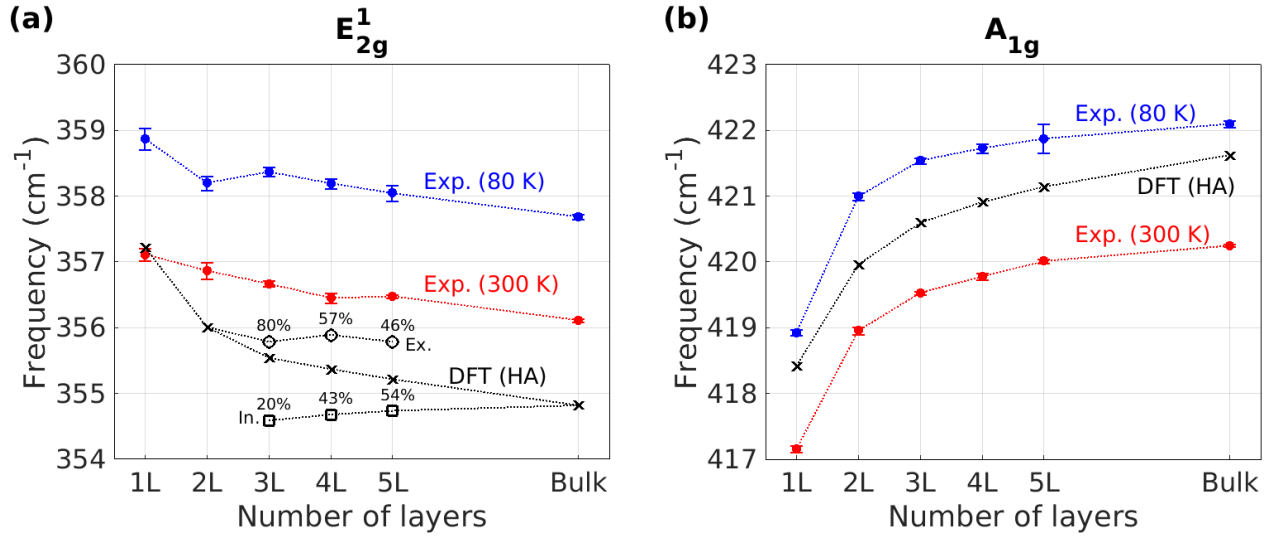


Fig. 3. Evolution of the E_{2g}^1 (a) and A_{1g} (b) phonon mode frequencies in WS_2 as a function of number of layers. The figure presents simulated frequencies (“DFT”) under harmonic approximation and experimental data (“Exp.”) for exfoliated samples at the temperatures of 80 K and 300 K. In the case of three and more WS_2 layers, the interior (“In”) and exterior (“Ex”) simulated phonon modes, their relative Raman intensities, and the averaged band positions (“x” symbols) are depicted.

To validate the simulated phonon structure of the multi-layered WS_2 films, we measured Raman spectra for the exfoliated samples (see the section 4) and fitted Voigt profiles to the observed bands (see the section 1.2 in *Supplementary Information*). To obtain the most distinct signal and reduce resonant scattering in the vicinity of the desired first-order phonon modes, we used a 785-nm laser line for the E_{2g}^1 mode and 514-nm for the A_{1g} mode. The spectra obtained at 80 K and 300 K temperatures are presented in Fig. 4 and Fig. S1, respectively, and the corresponding band positions in Fig. 3 and Tab. S1. With an increasing film thickness, we observe a redshift of the E_{2g}^1 mode and a blueshift of the A_{1g} mode, which are nearly independent of the temperature. The frequency shift of the A_{1g} mode agrees very well with the experimental data, but the calculated change of the E_{2g}^1 mode is overestimated. We also performed a similar study for the A_{1g} phonon mode in the CVD-grown WS_2 samples (at a 514-nm laser line) and obtained similar band positions but slightly blueshifted compared to the exfoliated samples – see the section 1.1.2 in *Supplementary Information*. We note that although the simulation within harmonic approximation is expected to describe phonon properties at 0 K properly, the DFT method itself is ambiguous due to the choice of exchange-correlation functional (see the section 2.1 in *Supplementary Information*), leading to shifts in the calculated phonon frequencies as observed in Fig. 3 with reference to the experiment. Therefore, relative differences are of the main interest.

Interestingly, at low temperatures, we observed additional Raman bands in the vicinity of the A_{1g} phonon mode (using a 514-nm laser line), which can be attributed to the split phonon modes in multi-layered WS_2 and were previously observed in resonant conditions using the 633-nm laser line [47]. Here, the effect might be due to the tensile strain of the bottom WS_2 layer caused by lattice mismatch between WS_2 and SiO_2 substrate at very low temperatures [48]. It was reported that such stress might not be fully transferred to the upper film layers [49,50], resulting in the vertical distribution of lattice constant. In the case of the E_{2g}^1 Raman band (using a 785-nm laser line), we observe an additional shoulder (here, attributed to 2LA(M) mode) whose intensity increases with the temperature (see Fig. S1) and the number of WS_2 layers.

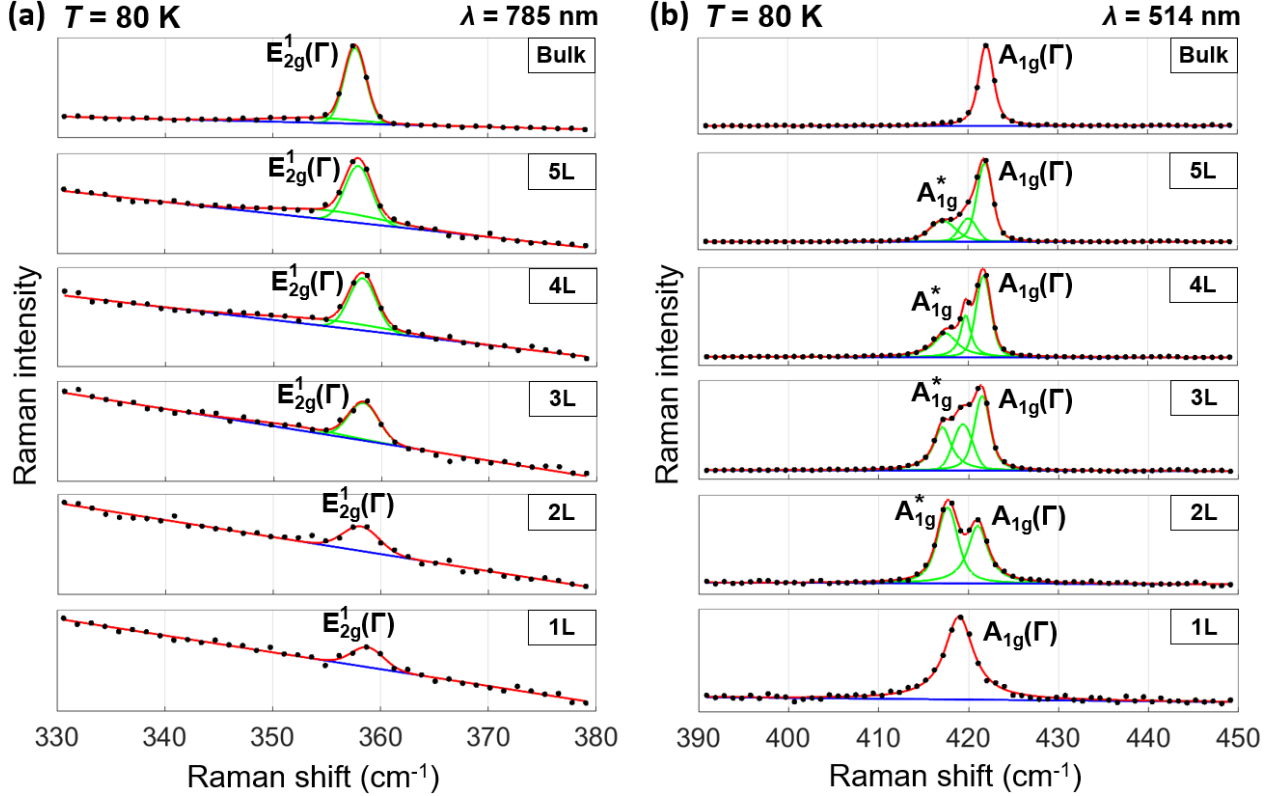


Fig. 4. Raman spectra of 1–5 layered exfoliated WS₂ films and bulk measured at the temperature of 80 K in the vicinity of the Raman active modes: (a) E_{2g}¹, (b) A_{1g}. The fitted Voigt profiles to the Raman bands are also presented.

2.2. Effect of the substrate on phonons – harmonic approximation

The above simulations were performed for free-standing WS₂ nanosheets, which is incomplete to study the properties of the film on the substrate. It has already been reported that the impact of the substrate on the frequencies of optical phonons can be significant [22,51], which is caused by doping (charge transfer from the substrate) and strain (due to lattice mismatch). The former effect has been more significant for the out-of-plane A_{1g} mode and the latter for the in-plane E_{2g}¹ mode. To study the substrate effect quantitatively in multi-layered WS₂, we extended the harmonic Γ -point simulations considering strained structures (tensile hydrostatic strain, up to 0.5% in each direction) with excess electron density (up to 10¹³/cm² per layer) – the same in each WS₂ layer. Those values correspond to the range of variation for MoS₂ monolayers supported on different substrates [52]. Each considered structure was individually relaxed, resulting in an additional effect on phonon frequencies. The simulated frequency shifts are presented in the form of two-dimensional maps for 1–2 layered WS₂ (Fig. 5) and compact form for 1–5 layered WS₂ films (Tab. 1).

Fig. 5 indicates that although the individual changes due to strain and doping are linear, the cumulated effect of both factors can generally be non-linear if the stress and excess charge are significant – contrary to what is usually assumed [52,53]. The strain-induced shifts of the E_{2g}¹ and A_{1g} phonons do not depend on the number of layers and are equal to about -3.6 cm⁻¹/% and -1.3 cm⁻¹/%, respectively. The effect is the same for individual split interior and exterior E_{2g}¹ modes in *n*L-WS₂ with *n* ≥ 3. The results align with the previous experimental and ab-initio study of hydrostatic strain and corresponding Grüneisen parameters [54]. Contrary, the redshift caused by the same excess electron concentration per WS₂ layer depends on the film thickness and is the most significant in thin WS₂ films. In the monolayer case, the A_{1g}

phonon frequency decreases by about 6 cm^{-1} upon $10^{13}/\text{cm}^2$ electron doping, which is of the order of the result obtained for electron-doped MoS_2 [21]. However, the same concentration per WS_2 layer has an insignificant impact in multi-layered films – the shift is reduced to about -0.3 cm^{-1} . In the case of the E_{2g}^1 mode, the corresponding change is -1.5 cm^{-1} for 1L- and 2L- WS_2 , while for three or more layers, the doping-induced changes are less significant and different for the interior and exterior modes – equal to about -1.0 and -0.5 cm^{-1} , respectively. The intensity ratio of the split E_{2g}^1 modes is also affected, further lowering the position of the observed Raman bands. The simulation indicates that for multi-layered WS_2 , the doping-induced shifts of E_{2g}^1 modes are more significant than of A_{1g} . This is contrary to the experimental result for 5.9-nm-thick WS_2 film [55] – the discrepancy with the reported observation might be due to an incorrect description of the doped samples with LDA parametrization of the XC functional (which overestimates the covalent part of inter-layer bonding [43]) or due to an inhomogeneous vertical charge distribution in the WS_2 film (as previously observed in bilayer graphene [49]). The non-uniform charge concentration might result in different force constants in different WS_2 layers, potentially causing an additional splitting of Raman bands.

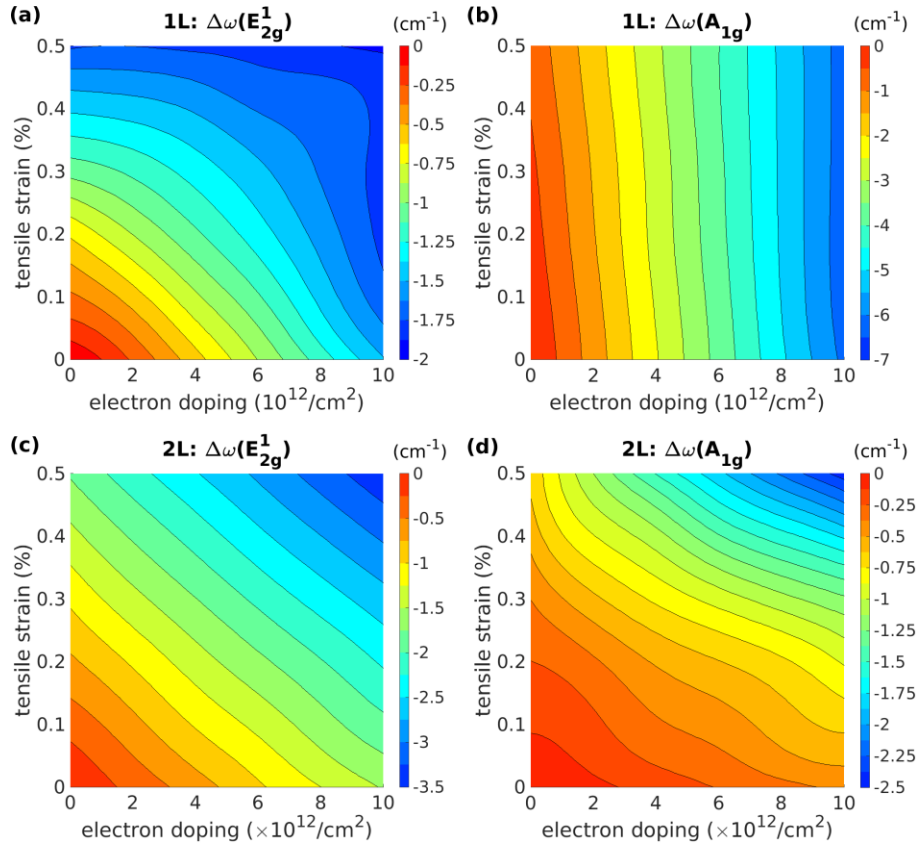


Fig. 5. Impact of the tensile strain and doping (excess electron concentration per WS_2 layer) on the energy of Raman active phonons in 1–2 layered WS_2 nanosheets: (a) E_{2g}^1 in 1L- WS_2 , (b) A_{1g} in 1L- WS_2 , (c) E_{2g}^1 in 2L- WS_2 , (d) A_{1g} in 2L- WS_2 .

Tab. 1. Effects of the biaxial strain ($\Delta\varepsilon = 0.5\%$) and electron-doping ($\Delta n = 10^{13}/\text{cm}^2$ per WS_2 layer) on harmonic frequencies of the E_{2g}^1 and A_{1g} phonon modes in WS_2 films with different numbers of layers. In the case of three and more WS_2 layers, the interior (“In”) and exterior (“Ex”) phonon modes are depicted, including their relative intensities (in curly braces).

	$\Delta\omega(E_{2g}^1) (\text{cm}^{-1})$		$\Delta\omega(A_{1g}) (\text{cm}^{-1})$	
	$\Delta\varepsilon = 0.5\%$	$\Delta n = 10^{13}/\text{cm}^2$	$\Delta\varepsilon = 0.5\%$	$\Delta n = 10^{13}/\text{cm}^2$
1L	-1.8	-1.5	-0.7	-6.1
2L	-1.8	-1.5	-0.6	-0.4
3L	In: -1.8 {21%} Ex: -1.8 {79%}	In: -0.9 {61%} Ex: -0.6 {39%}	-0.7	-0.3
4L	In: -1.8 {43%} Ex: -1.8 {57%}	In: -1.0 {70%} Ex: -0.5 {30%}	-0.6	-0.2
5L	In: -1.8 {55%} Ex: -1.8 {45%}	In: -0.9 {76%} Ex: -0.4 {24%}	-0.6	-0.4

2.3. Phonon anharmonicity

The above computational studies were performed under harmonic approximation, neglecting the dependence of the phonon propagation on the lattice thermal expansion and oscillation amplitude. However, the real interatomic potentials include higher-order anharmonic terms, which have a noticeable impact on phonon propagation by means of their energies and lifetimes. The anharmonicity affects the phonons by thermal expansion of the structure (mean positions between atoms increase with the temperature) and non-zero oscillation amplitude leading to interactions between phonons – mathematically described by shifts of energies and time-dependent occupations of the phonon eigenstates. This leads to the following temperature dependence of the Raman peak position $\omega_j(T)$ and its half-width $\Gamma_j(T)$ (inverse lifetime) corresponding to the $(\mathbf{0}, j)$ phonon mode:

$$\omega_j(T) = \omega_j^{\text{QHA}}(\{a_i(T)\}) + \Delta\omega_j^{\text{ph-ph}}(T) \Big|_{\{a_i(T)\}}, \quad \Gamma_j(T) = \Gamma_j^{\text{ph-ph}}(T) \Big|_{\{a_i(T)\}} \quad (1)$$

where $\omega_j^{\text{QHA}}(\{a_i(T)\})$ is the (quasi) harmonic frequency evaluated at the temperature-dependent geometry $\{a_i(T)\}$ of the crystal (due to thermal expansion), and the values $\Delta\omega_j^{\text{ph-ph}}(T)$, $\Gamma_j^{\text{ph-ph}}(T)$ (given by (S6) and (S7), respectively) represent quantum-mechanical corrections due to the phonon-phonon anharmonic interactions. We included the following three-phonon interaction processes in the model: the decay of the zero-momentum phonon into two phonons with opposite momenta or coalescence of the zero-momentum phonon with a second one to eject another phonon [56]. Note that the effect of phonon-phonon interactions in (1) can, in general, also be indirectly affected by the lattice thermal expansion. However, we found the mentioned difference to be negligible for the crystals studied in this paper – we recorded only a slight increase of the FWHM at the temperature of 500 K – not greater than 0.07 cm^{-1} – if we considered the thermally expanded lattice. Further details concerning evaluation of the phonon-phonon interactions and thermal expansion are described in the sections 2.3.1 and 2.3.2 in *Supplementary Information*, respectively. We did not include an effect of electron-phonon interactions due to the lack of electron states in the vicinity of the Fermi level [57] in semiconducting WS_2 . This assumption might be invalid in heavily doped WS_2 .

Following the above theoretical background, we performed ab-initio simulations of energy shift and corresponding bandwidth for the fundamental modes A_{1g} and E_{2g}^1 in 1–5 layered WS_2 films and bulk, as a function of temperature in the range from 0 to 500 K (see the section 3). We note that the temperature-dependent phonon energy evolution as a function of number of monolayers of WS_2 is demonstrated for the first time. Firstly, we simulated the temperature-dependent lattice parameters (Fig. S6): in-plane lattice constant, monolayer thickness, and interlayer distance. The corresponding thermal expansion coefficients are linear above 300 K and equal about $(5.8–6.2) \times 10^{-6}/K$, $(1.8–2.8) \times 10^{-6}/K$, and $(1.3–1.5) \times 10^{-5}/K$, respectively. The obtained thermal expansion of the in-plane lattice constant is consistent with the experimental [29,58] and first-principles reports [59,60]. Also, the ratio of coefficients corresponding to the interlayer distance and in-plane lattice constant – of the order of 2 – is similar to the values reported in other TMDCs with 2H structure [61,62]. Next, we studied the temperature evolution of the phonon properties – frequencies and bandwidths – including the impact of lattice thermal expansion and three-phonon interaction processes. In the case of split E_{2g}^1 interior and exterior modes in nL - WS_2 with $n \geq 3$, we evaluated each corresponding band position and FWHM as the weighted average with respect to the E_{2g}^1 Raman intensities (see Fig. S5). The exterior modes were slightly more anharmonic than the interior ones. The results, together with temperature-dependent experimental data for exfoliated WS_2 films, are presented in Fig. 6. For better clarity of comparison with the experimental data, we shifted each simulated curve by a temperature-independent constant. In the case of phonon frequency, such correction can be justified by the ambiguity of the results obtained with different XC parametrizations (see tests in Tab. S3) and by the substrate effects (see Fig. 5). The corrections of the bandwidths represent phonon dissipation effects not taken into account in the simulation, such as scattering on the substrate or defects. Individual changes in phonon energies and corresponding bandwidths caused by thermal expansion, phonon-phonon interactions, and both the effects are compared in Fig. S7. Additionally, frequency changes caused by expansion of individual geometrical parameters are depicted in Tab. S4. The impacts of the thermal expansion and phonon-phonon interactions on the temperature evolution of the A_{1g} and E_{2g}^1 modes are of a similar order.

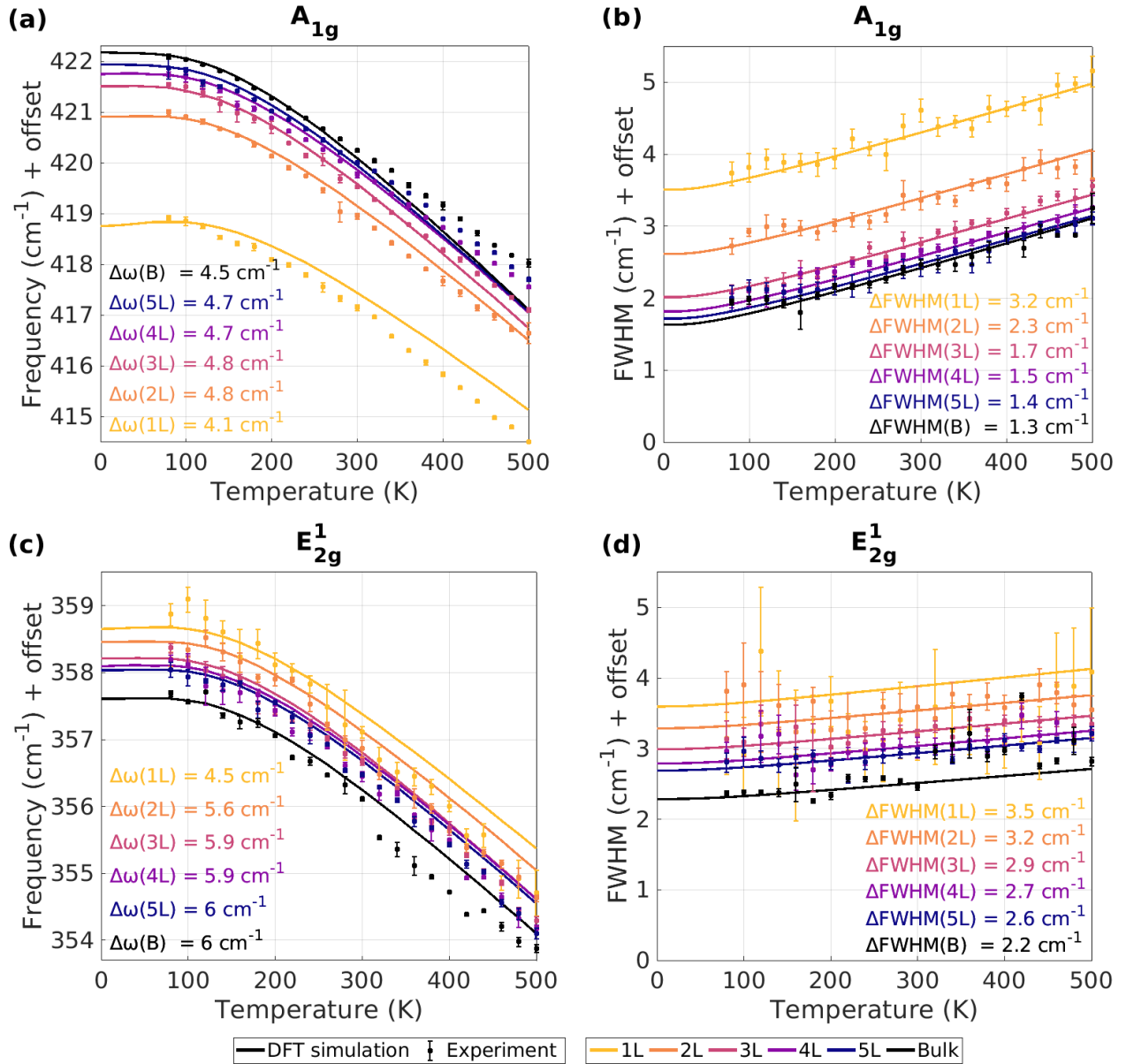


Fig. 6. Temperature dependence of the frequencies and full widths at half maximum of the A_{1g} (a-b) and E_{2g}^1 (c-d) phonon modes in 1–5 layered and bulk WS_2 as obtained with DFT simulation and Raman experiment for exfoliated samples. For better comparison with the experimental data, the simulation results are shifted by additive constants (depicted in the figure).

The experimental temperature dependences of frequencies and bandwidths corresponding to the A_{1g} and E_{2g}^1 phonon modes agree well with the simulation results, although only temperature-independent constants were added. This is a significant improvement over the recently reported DFT study of phonon anharmonicity in 1-2 layered MoS_2 [36], where both additive and multiplicative corrections had to be used to obtain the agreement between experimental and computational data – probably due to the choice of XC parametrization or pseudopotentials. However, we observe a slight underestimation (overestimation) of the simulated temperature-dependent slope of the A_{1g} phonon energy in monolayer WS_2 (multi-layered WS_2) compared to the experimental results. It might be due to the effects of four-phonon interaction processes or charge doping from the substrate, which are not included in our model. The trend is linear above 300 K – the simulated slope equals $-0.0115 \text{ cm}^{-1}/\text{K}$ in 1L- WS_2 , $-0.0132 \text{ cm}^{-1}/\text{K}$ in 2L- WS_2 , and grows

to $-0.0149 \text{ cm}^{-1}/\text{K}$ in bulk WS_2 , while the experimental slope equals $-0.0133 \text{ cm}^{-1}/\text{K}$ in monolayer and reduces to $-0.0115 \text{ cm}^{-1}/\text{K}$ in bulk WS_2 . We also obtained similar experimental results for the CVD-grown samples on SiO_2/Si substrate (Fig. S4) – however, the widths of the measured Raman bands are greater than in the exfoliated samples. We checked that the difference in the simulated temperature-induced slopes of the A_{1g} mode is mainly due to thermal expansion in the WS_2 films – particularly the expansion of the distance between WS_2 layers. In the case of the E_{2g}^1 phonon mode energy, the simulated slopes are slightly underestimated for any multi-layered WS_2 – they are equal from $-0.0107 \text{ cm}^{-1}/\text{K}$ in bulk WS_2 to $0.0100 \text{ cm}^{-1}/\text{K}$ in monolayer, and the experimental slopes – from $-0.0121 \text{ cm}^{-1}/\text{K}$ in the monolayer to $-0.0104 \text{ cm}^{-1}/\text{K}$ in bulk. In the case of the bandwidths, the temperature trends almost do not change with the number of layers, but significant thickness-dependent constant shifts are observed. The total bandwidth increases with decreasing number of layers, which can be attributed to scattering (leakage) of out-of-plane A_{1g} phonons on the substrate [63]. The effect of substrate on the phonon bandwidths has been previously reported for MoS_2 [36,64] – the in-plane E_{2g}^1 phonons are much less affected by the substrate than the out-of-plane A_{1g} modes. The influence of the phonon leakage on the substrate is not included in the model – a further study using a larger supercell with substrate atoms is needed to investigate this effect.

The general formula (1) describing the temperature dependence of the phonon parameters used in the above study does not include interaction with the substrate. The impact of the induced strain can be taken into account by considering additional potential energy terms or using additional constraints for the geometrical degrees of freedom. However, other effects – e.g., charge doping and phonons leakage into the substrate – have to be considered either indirectly (as relevant additive corrections) or by including substrate atoms in the model (significantly increasing computational cost). Moreover, one should be aware of defects formation, which might, in general, also affect the phonon frequencies and lifetimes. Here, we performed a study for single-layered WS_2 with sulfur vacancies (see the section 2.4 in *Supplementary Information*) – we recorded slight shifts of the E_{2g}^1 and A_{1g} phonon frequencies below 0.13 cm^{-1} and an increase of FWHM of both the modes by about 0.3 cm^{-1} for vacancies concentration of 1%.

3. Computational details

3.1. General details

All simulations were based on the DFT method as implemented in SIESTA MaX-1.0-17 software [65,66], which uses localized basis functions and, therefore, is highly advantageous for two-dimensional structures and large systems. We used LDA parametrization [67] of the exchange-correlation (XC) functional and scalar relativistic pseudopotentials available at the Pseudo-Dojo database [68] (type ONCVSP v0.4.1, PSML format) [69,70]. However, we also tested other XC functionals and the correction scheme for van der Waals interactions – and found them less appropriate to reproduce the experimental phonon frequencies (see the section 2.1 in *Supplementary Information*). DZP basis sets (double- ζ with polarization) were applied, and radii of basis orbitals were increased by setting the corresponding internal “energy shift” parameter [66] equal to 1×10^{-4} Ry. To reduce an “eggbox effect” [65], we applied filtering of the basis functions [65] with the cutoff set to 500 Ry.

3.2. Phonons in harmonic approximation

To study dispersion and ionic displacements corresponding to the phonon modes in WS_2 nanosheets, all the slabs (up to five WS_2 layers) were modeled utilizing unit cells of the height 50 \AA , which

contained corresponding WS₂ layers (arranged in the structure of 2H-WS₂ bulk) and appropriate vacuum separation between periodic images. In contrast, in the case of the bulk 2H-WS₂, we used a unit cell with two WS₂ layers (see Fig. 1a) and utilized the vertical periodicity. Structure optimizations were performed in 1×1×1 unit cells, and the thresholds were set equal to 0.001 eV/Å for atomic forces and 0.001 GPa for stress tensor components. Second-order interatomic force constants were calculated utilizing the central finite difference method with displacements of 0.05 Å using 7×7×1 supercells (147 atoms per WS₂ layer) for slabs and 7×7×3 for bulk (six WS₂ layers). We applied Γ -centered 14×14×1 (14×14×6) \mathbf{k} -point grid for slabs (bulk) and 2000 Ry cutoff of real-space mesh for calculations utilizing 1×1×1 unit cell (structure optimizations and Γ -point phonon calculations), whereas for simulations using supercells (studies of phonon dispersion $\omega_{\mathbf{q},j}$ and defected WS₂) 1×1×1 \mathbf{k} -point grid and 500 Ry mesh cutoff were sufficient. Phonon densities of states were evaluated with 200×200×1 \mathbf{q} -point grids for slabs and 200×200×10 for the bulk of pristine WS₂.

3.3. Phonon anharmonicity

To calculate theoretical shifts and linewidths of each of the desired phonons ($\mathbf{0}, j$), caused by the phonon-phonon interactions in (1), we evaluated the third-order coefficients $V^{(3)}(\mathbf{0}, j; -\mathbf{q}, j_1; \mathbf{q}, j_2)$ utilizing the method based on the frozen-phonon approach [71] as presented in the section 2.3.1 in *Supplementary Information*. The applied value of the distortion magnitude Δu in (S8) was equal to $\sqrt{n} \times 0.05$ Å, where n is the number of W atoms in the unit cell – to provide similar values of the real-space atomic displacements. Then, we evaluated an ancillary function $\tilde{I}_j(\omega')$, which is expressed with the same formula as in (S7) but with ω' substituted for ω . The function $\tilde{I}_j(\omega')$ was calculated by integration over the first BZ using a tetrahedron method [72] with a 70×70×1 \mathbf{q} -point grid for slabs and 70×70×10 for bulk. In the case of the defects study (in 7×7×1 supercells), the integration was performed with a 10×10×1 \mathbf{q} -point grid. Finally, $I_j^{\text{ph-ph}} = \tilde{I}_j(\omega_{\mathbf{0},j})$. For convenience, the integral in (S6) representing the value of $\Delta\omega_j^{\text{ph-ph}}$ was evaluated using the Kramers–Kronig relation (please be aware of the signs of the real and imaginary parts of the proper self-energy [34]):

$$\Delta\omega_j^{\text{ph-ph}} = \frac{2}{\pi} \times P \int_0^{+\infty} \frac{-\tilde{I}_j(\omega')\omega' d\omega'}{\omega'^2 - \omega_{\mathbf{0},j}^2}, \quad (2)$$

where P denotes the Cauchy principal value. For convenience, the integral in (2) can be simplified by a substitution $\omega' = \sqrt{\xi}$, which results in $\Delta\omega_j^{\text{ph-ph}} = -\frac{1}{\pi} \times P \int_0^{+\infty} \tilde{I}_j(\sqrt{\xi}) d\xi / (\xi - \omega_{\mathbf{0},j}^2)$. Moreover, one can consider two separate integrals over the intervals $[0, \omega_{\mathbf{0},j}^2 - \varepsilon]$ and $[\omega_{\mathbf{0},j}^2 + \varepsilon, +\infty)$, where $\varepsilon \rightarrow 0^+$, and substitute $\xi = \omega_{\mathbf{0},j}^2 - \varepsilon e^t$ and $\xi = \omega_{\mathbf{0},j}^2 + \varepsilon e^t$ in the first and second integral respectively, which results in the final simple formula for $\Delta\omega_j^{\text{ph-ph}}$:

$$\Delta\omega_j^{\text{ph-ph}} = \lim_{\varepsilon \rightarrow 0^+} \left(\frac{1}{\pi} \int_0^{\ln(\omega_{\mathbf{0},j}^2/\varepsilon)} \tilde{I}_j \left(\sqrt{\omega_{\mathbf{0},j}^2 - \varepsilon e^t} \right) dt - \frac{1}{\pi} \int_0^{+\infty} \tilde{I}_j \left(\sqrt{\omega_{\mathbf{0},j}^2 + \varepsilon e^t} \right) dt \right). \quad (3)$$

To study the thermal expansion effects, as described in the section 2.3.2 in *Supplementary Information*, the Helmholtz free energy (S16) was minimized with respect to relative changes $\varepsilon_a = \Delta a/a$, $\varepsilon_d = \Delta d/d$, $\varepsilon_c = \Delta c/c$ of the three geometrical parameters: in-plane lattice constant, thickness of individual WS₂ layer (S-S), and distance between two closest monolayers (W-W). Note that the depicted dimensions do not have to be the same for each layer in the slab, which justifies the use of relative changes.

The first term of (S16) was calculated in the domain $(\varepsilon_a, \varepsilon_d, \varepsilon_c) \in [0, 0.5\%] \times [0, 0.5\%] \times [0, 1.0\%]$ on a uniform $6 \times 6 \times 5$ grid, and the second term (which we found to be a linear function of the $\varepsilon_a, \varepsilon_d, \varepsilon_c$ parameters) on a $2 \times 2 \times 2$ grid. In the case of the monolayer, no separate dimension for ε_c was considered. Integrations over the first BZ were performed with the same meshes as used to evaluate the densities of states (for defected $7 \times 7 \times 1$ supercells, we used $30 \times 30 \times 1$ q -point grids). The function (S16) was interpolated over a dense grid, and the position of its minimum was found for temperatures in the range 0–500 K, which revealed the temperature-dependent lattice parameters. Quasi-harmonic Γ -point phonon frequencies were then calculated in the above-depicted domain on a $2 \times 2 \times 2$ grid (2×2 for the monolayer) and interpolated for the desired temperature-dependent lattice parameters.

4. Experimental details

Exfoliated samples were prepared using a gold-assisted exfoliation process from 2H-WS₂ bulk sample purchased from SPI supplier [73]. The number of layers was determined by a combination of optical contrast, AFM thickness measurements, photoluminescence and Raman spectra at room temperature. For details of CVD-grown samples and thickness-dependent properties, see the section 1.1 in *Supplementary Information*. The illustration of the 2H-WS₂ structure (Fig. 1a) was created using VESTA software [74].

Raman measurements were performed using Renishaw inVia Qontor spectrometer in backscattering configuration. All spectra were collected using the 514 nm (with 3000 lines/mm grating) and 785 nm (with 1200 lines/mm grating) laser lines with circularly polarized light, 50 \times long distance objective with $NA = 0.5$. The resolution of the Raman system is less than 1 cm^{-1} . Laser power on the sample was measured using the Ophir Nova II system and was kept below 0.1 mW for 514 nm laser to minimize heating and light-induced damage. All measurements were done in Oxford Microstat He cryostat in a high vacuum (better than 1×10^{-5} mbar). The system was cooled down with liquid nitrogen and offered temperature stability of 0.1 K. During temperature-dependent Raman measurement, 10 minutes of stabilization time was applied to reach thermal equilibrium after setting temperature. To obtain low noise, the high-quality spectra acquisition time was set to 30 s for each measurement. Moreover, each measurement was repeated two times for the exfoliated and three times for the CVD-grown samples to further minimize measurement uncertainty. AFM measurements were performed using Bruker Dimension Icon microscope with general-purpose ScanAsyst imaging mode and Sanyasis-Air probes with a nominal tip radius of 2 nm.

5. Conclusions

We performed a comprehensive study of phonon properties in multi-layered WS₂ using a combination of temperature-dependent Raman (80–500 K) and DFT (0–500 K) approaches and explored the impact of the number of layers on harmonic and anharmonic properties of in-plane E_{2g}¹ and out-of-plane A_{1g} vibrations. Additionally, we simulated the dependence of the phonon harmonic frequencies on the cumulated strain and doping – substrate-induced effects. Our work makes the following principal findings:

- First-principles model based on a DFT approach including three-phonon anharmonic interaction processes and the system’s thermal expansion can reliably reproduce experimental temperature-induced evolution of phonon frequencies and lifetimes, giving a great promise of using the models to investigate vibrational properties and heat transport in multi-layered WS₂ and similar 2D materials.

- The models of anharmonicity predict a relatively large increase in the temperature-induced shift of out-of-plane vibrations' frequency in multi-layered WS₂ – the simulated slope above room temperature increases from -0.011 cm⁻¹/K in monolayer WS₂ to -0.015 cm⁻¹/K in bulk. We attributed the difference primarily to the thermal expansion of the interlayer distance.
- The lifetime of the out-of-plane phonons is significantly reduced in thin samples by interaction with the substrate – the more layers in the film, the larger the phonon lifetime. However, the temperature-induced changes do not depend on the film thickness.
- Electron doping (e.g., from the substrate) significantly affects out-of-plane vibrations in monolayer WS₂ while having little influence in thicker samples. Contrary, the effect of biaxial strain is more significant in the in-plane phonon mode and independent of the number of layers.
- Anharmonicity of in-plane phonons in layered materials is nearly unaffected by the film thickness – the corresponding temperature-dependent slope above room temperature equals about -0.010 cm⁻¹/K for any number of layers.

Data availability

The data that support the findings of this study are available from the corresponding author upon reasonable request.

Code availability

All non-commercial numerical codes to reproduce the findings of this study are available from the corresponding author upon reasonable request.

Acknowledgements

The authors acknowledge the support of the EU Graphene Flagship funding (Grant Graphene Core3 n° 881603). The research was realized as part of two PRELUDIUM (UMO-2019/33/N/ST5/01414 and UMO-2019/35/N/ST5/00742) projects, funded by the Polish National Science Centre (NCN). We also acknowledge the usage of computer cluster DWARF at Warsaw University of Technology supported by the Polish National Science Center (NCN) under Contracts No. UMO-2017/26/E/ST3/00428 and UMO-2017/27/B/ST2/02792.

Author contributions

KW and APG conceived and designed the study, and analyzed the data. KW performed DFT calculations, and prepared the manuscript. APG, KÇ and JS fabricated the samples and performed Raman measurements. MZ supervised the study. The manuscript was written through the contributions of all authors. All authors have approved the final version of the manuscript.

Competing interest

The authors declare no competing interests.

References

- [1] J. Ding, A. Feng, X. Li, S. Ding, L. Liu, W. Ren, Properties, preparation, and application of tungsten disulfide: a review, *J. Phys. D: Appl. Phys.* 54 (2021) 173002. <https://doi.org/10.1088/1361-6463/abd9e8>.
- [2] S. Manzeli, D. Ovchinnikov, D. Pasquier, O.V. Yazyev, A. Kis, 2D transition metal dichalcogenides, *Nat Rev Mater.* 2 (2017) 1–15. <https://doi.org/10.1038/natrevmats.2017.33>.

- [3] Q.H. Wang, K. Kalantar-Zadeh, A. Kis, J.N. Coleman, M.S. Strano, Electronics and optoelectronics of two-dimensional transition metal dichalcogenides, *Nature Nanotech.* 7 (2012) 699–712. <https://doi.org/10.1038/nnano.2012.193>.
- [4] W. Choi, N. Choudhary, G.H. Han, J. Park, D. Akinwande, Y.H. Lee, Recent development of two-dimensional transition metal dichalcogenides and their applications, *Materials Today.* 20 (2017) 116–130. <https://doi.org/10.1016/j.mattod.2016.10.002>.
- [5] Z. Wei, B. Li, C. Xia, Y. Cui, J. He, J.-B. Xia, J. Li, Various Structures of 2D Transition-Metal Dichalcogenides and Their Applications, *Small Methods.* 2 (2018) 1800094. <https://doi.org/10.1002/smt.201800094>.
- [6] Y. Wang, C. Cong, W. Yang, J. Shang, N. Peimyoo, Y. Chen, J. Kang, J. Wang, W. Huang, T. Yu, Strain-induced direct–indirect bandgap transition and phonon modulation in monolayer WS₂, *Nano Res.* 8 (2015) 2562–2572. <https://doi.org/10.1007/s12274-015-0762-6>.
- [7] F. Zhang, Y. Lu, D.S. Schulman, T. Zhang, K. Fujisawa, Z. Lin, Y. Lei, A.L. Elias, S. Das, S.B. Sinnott, M. Terrones, Carbon doping of WS₂ monolayers: Bandgap reduction and p-type doping transport, *Science Advances.* 5 (2019) eaav5003. <https://doi.org/10.1126/sciadv.aav5003>.
- [8] W. Li, T. Wang, X. Dai, X. Wang, C. Zhai, Y. Ma, S. Chang, Bandgap engineering of different stacking WS₂ bilayer under an external electric field, *Solid State Communications.* 225 (2016) 32–37. <https://doi.org/10.1016/j.ssc.2015.10.013>.
- [9] N.A.N. Phan, H. Noh, J. Kim, Y. Kim, H. Kim, D. Whang, N. Aoki, K. Watanabe, T. Taniguchi, G.-H. Kim, Enhanced Performance of WS₂ Field-Effect Transistor through Mono and Bilayer h-BN Tunneling Contacts, *Small.* 18 (2022) 2105753. <https://doi.org/10.1002/sml.202105753>.
- [10] S.J. Kim, D. Kim, B.K. Min, Y. Yi, S. Mondal, V.-T. Nguyen, J. Hwang, D. Suh, K. Cho, C.-G. Choi, Bandgap Tuned WS₂ Thin-Film Photodetector by Strain Gradient in van der Waals Effective Homo Junctions, *Advanced Optical Materials.* 9 (2021) 2101310. <https://doi.org/10.1002/adom.202101310>.
- [11] M. Shanmugam, T. Bansal, C.A. Durcan, B. Yu, Schottky-barrier solar cell based on layered semiconductor tungsten disulfide nanofilm, *Appl. Phys. Lett.* 101 (2012) 263902. <https://doi.org/10.1063/1.4773525>.
- [12] B. Wei, Q. Sun, C. Li, J. Hong, Phonon anharmonicity: a pertinent review of recent progress and perspective, *Sci. China Phys. Mech. Astron.* 64 (2021) 117001. <https://doi.org/10.1007/s11433-021-1748-7>.
- [13] Y. Quan, S. Yue, B. Liao, Impact of Electron-Phonon Interaction on Thermal Transport: A Review, *Nanoscale and Microscale Thermophysical Engineering.* 25 (2021) 73–90. <https://doi.org/10.1080/15567265.2021.1902441>.
- [14] G. Qin, Z. Qin, H. Wang, M. Hu, Lone-pair electrons induced anomalous enhancement of thermal transport in strained planar two-dimensional materials, *Nano Energy.* 50 (2018) 425–430. <https://doi.org/10.1016/j.nanoen.2018.05.040>.
- [15] Y. Yu, M. Cagnoni, O. Cojocaru-Miréidin, M. Wuttig, Chalcogenide Thermoelectrics Empowered by an Unconventional Bonding Mechanism, *Advanced Functional Materials.* 30 (2020) 1904862. <https://doi.org/10.1002/adfm.201904862>.
- [16] M.A. Avila, K. Suekuni, K. Umeo, H. Fukuoka, S. Yamanaka, T. Takabatake, Ba₈Ga₁₆Sn₃₀ with type-I clathrate structure: Drastic suppression of heat conduction, *Appl. Phys. Lett.* 92 (2008) 041901. <https://doi.org/10.1063/1.2831926>.
- [17] X. Gu, R. Yang, Phonon transport and thermal conductivity in two-dimensional materials, *Annual Review of Heat Transfer.* 19 (2016). <https://doi.org/10.1615/AnnualRevHeatTransfer.2016015491>.
- [18] X. Zhang, X.-F. Qiao, W. Shi, J.-B. Wu, D.-S. Jiang, P.-H. Tan, Phonon and Raman scattering of two-dimensional transition metal dichalcogenides from monolayer, multilayer to bulk material, *Chemical Society Reviews.* 44 (2015) 2757–2785. <https://doi.org/10.1039/C4CS00282B>.

- [19] S. Bae, N. Sugiyama, T. Matsuo, H. Raebiger, K. Shudo, K. Ohno, Defect-Induced Vibration Modes of Ar+-Irradiated MoS₂, *Phys. Rev. Applied.* 7 (2017) 024001. <https://doi.org/10.1103/PhysRevApplied.7.024001>.
- [20] M. Staiger, P. Rafailov, K. Gartsman, H. Telg, M. Krause, G. Radovsky, A. Zak, C. Thomsen, Excitonic resonances in WS₂ nanotubes, *Phys. Rev. B.* 86 (2012) 165423. <https://doi.org/10.1103/PhysRevB.86.165423>.
- [21] B. Chakraborty, A. Bera, D.V.S. Muthu, S. Bhowmick, U.V. Waghmare, A.K. Sood, Symmetry-dependent phonon renormalization in monolayer MoS₂ transistor, *Phys. Rev. B.* 85 (2012) 161403. <https://doi.org/10.1103/PhysRevB.85.161403>.
- [22] M.W. Iqbal, K. Shahzad, R. Akbar, G. Hussain, A review on Raman finger prints of doping and strain effect in TMDCs, *Microelectronic Engineering.* 219 (2020) 111152. <https://doi.org/10.1016/j.mee.2019.111152>.
- [23] W. Zhao, Z. Ghorannevis, K. Kumar Amara, J. Ren Pang, M. Toh, X. Zhang, C. Kloc, P. Heng Tan, G. Eda, Lattice dynamics in mono- and few-layer sheets of WS₂ and WSe₂, *Nanoscale.* 5 (2013) 9677–9683. <https://doi.org/10.1039/C3NR03052K>.
- [24] S. Zhu, W. Zheng, Temperature-Dependent Phonon Shifts in van der Waals Crystals, *J. Phys. Chem. Lett.* 12 (2021) 5261–5270. <https://doi.org/10.1021/acs.jpcclett.1c00947>.
- [25] H. Gu, K. Chen, X. Gao, K. Xu, Y. Lu, X. Liu, Temperature- and position-dependent Raman study on carrier concentration of large-area monolayer WS₂, *Applied Surface Science.* 481 (2019) 241–245. <https://doi.org/10.1016/j.apsusc.2019.03.127>.
- [26] N. Peimyoo, J. Shang, W. Yang, Y. Wang, C. Cong, T. Yu, Thermal conductivity determination of suspended mono- and bilayer WS₂ by Raman spectroscopy, *Nano Res.* 8 (2015) 1210–1221. <https://doi.org/10.1007/s12274-014-0602-0>.
- [27] S. Sinha, V. Sathe, S.K. Arora, Temperature dependent Raman investigations of few-layered WS₂ nanosheets, *Solid State Communications.* 298 (2019) 113626. <https://doi.org/10.1016/j.ssc.2019.04.013>.
- [28] A.P. Gertych, K. Czerniak-Łosiewicz, A. Łapińska, M. Świniarski, M. Ojrzyńska, J. Judek, M. Zdrojek, Phonon and Thermal Properties of Thin Films Made from WS₂ Mono- and Few-Layer Flakes, *J. Phys. Chem. C.* 125 (2021) 14446–14452. <https://doi.org/10.1021/acs.jpcc.1c02842>.
- [29] H. Zobeiri, S. Xu, Y. Yue, Q. Zhang, Y. Xie, X. Wang, Effect of temperature on Raman intensity of nm-thick WS₂: combined effects of resonance Raman, optical properties, and interface optical interference, *Nanoscale.* 12 (2020) 6064–6078. <https://doi.org/10.1039/C9NR10186A>.
- [30] Y.-K. Peng, Z.-Y. Cao, L.-C. Chen, N. Dai, Y. Sun, X.-J. Chen, Phonon Anharmonicity of Tungsten Disulfide, *J. Phys. Chem. C.* 123 (2019) 25509–25514. <https://doi.org/10.1021/acs.jpcc.9b07553>.
- [31] Z. Lin, W. Liu, S. Tian, K. Zhu, Y. Huang, Y. Yang, Thermal expansion coefficient of few-layer MoS₂ studied by temperature-dependent Raman spectroscopy, *Sci Rep.* 11 (2021) 7037. <https://doi.org/10.1038/s41598-021-86479-6>.
- [32] J. Park, Y. Kim, Y.I. Jhon, Y.M. Jhon, Temperature dependent Raman spectroscopic study of mono-, bi-, and tri-layer molybdenum ditelluride, *Appl. Phys. Lett.* 107 (2015) 153106. <https://doi.org/10.1063/1.4934181>.
- [33] Z. Li, Y. Wang, J. Jiang, Y. Liang, B. Zhong, H. Zhang, K. Yu, G. Kan, M. Zou, Temperature-dependent Raman spectroscopy studies of 1–5-layer WSe₂, *Nano Res.* 13 (2020) 591–595. <https://doi.org/10.1007/s12274-020-2669-0>.
- [34] M. Balkanski, R.F. Wallis, E. Haro, Anharmonic effects in light scattering due to optical phonons in silicon, *Phys. Rev. B.* 28 (1983) 1928–1934. <https://doi.org/10.1103/PhysRevB.28.1928>.
- [35] X. Huang, Y. Gao, T. Yang, W. Ren, H.-M. Cheng, T. Lai, Quantitative Analysis of Temperature Dependence of Raman shift of monolayer WS₂, *Sci Rep.* 6 (2016) 32236. <https://doi.org/10.1038/srep32236>.

- [36] S. Sarkar, I. Maity, H.L. Pradeepa, G. Nayak, L. Marty, J. Renard, J. Coraux, N. Bendiab, V. Bouchiat, S. Das, K. Majumdar, M. Jain, A. Bid, Anharmonicity in Raman-active phonon modes in atomically thin MoS₂, *Phys. Rev. B.* 101 (2020) 205302. <https://doi.org/10.1103/PhysRevB.101.205302>.
- [37] D. Tristant, A. Cupo, X. Ling, V. Meunier, Phonon Anharmonicity in Few-Layer Black Phosphorus, *ACS Nano.* 13 (2019) 10456–10468. <https://doi.org/10.1021/acsnano.9b04257>.
- [38] N. Bonini, M. Lazzeri, N. Marzari, F. Mauri, Phonon Anharmonicities in Graphite and Graphene, *Phys. Rev. Lett.* 99 (2007) 176802. <https://doi.org/10.1103/PhysRevLett.99.176802>.
- [39] D.J. Late, S.N. Shirodkar, U.V. Waghmare, V.P. Dravid, C.N.R. Rao, Thermal Expansion, Anharmonicity and Temperature-Dependent Raman Spectra of Single- and Few-Layer MoSe₂ and WSe₂, *ChemPhysChem.* 15 (2014) 1592–1598. <https://doi.org/10.1002/cphc.201400020>.
- [40] A. Mobaraki, A. Kandemir, H. Yapicioglu, O. Gülseren, C. Sevik, Validation of inter-atomic potential for WS₂ and WSe₂ crystals through assessment of thermal transport properties, *Computational Materials Science.* 144 (2018) 92–98. <https://doi.org/10.1016/j.commatsci.2017.12.005>.
- [41] P.Y. Yu, M. Cardona, *Fundamentals of Semiconductors*, Springer Berlin Heidelberg, Berlin, Heidelberg, 2010. <https://doi.org/10.1007/978-3-642-00710-1>.
- [42] J. Yang, J.-U. Lee, H. Cheong, Excitation energy dependence of Raman spectra of few-layer WS₂, *FlatChem.* 3 (2017) 64–70. <https://doi.org/10.1016/j.flatc.2017.06.001>.
- [43] A. Molina-Sánchez, L. Wirtz, Phonons in single-layer and few-layer MoS₂ and WS₂, *Phys. Rev. B.* 84 (2011) 155413. <https://doi.org/10.1103/PhysRevB.84.155413>.
- [44] X. Luo, Y. Zhao, J. Zhang, Q. Xiong, S.Y. Quek, Anomalous frequency trends in MoS₂ thin films attributed to surface effects, *Phys. Rev. B.* 88 (2013) 075320. <https://doi.org/10.1103/PhysRevB.88.075320>.
- [45] H. Terrones, E.D. Corro, S. Feng, J.M. Poumirol, D. Rhodes, D. Smirnov, N.R. Pradhan, Z. Lin, M. a. T. Nguyen, A.L. Elías, T.E. Mallouk, L. Balicas, M.A. Pimenta, M. Terrones, New First Order Raman-active Modes in Few Layered Transition Metal Dichalcogenides, *Sci Rep.* 4 (2014) 4215. <https://doi.org/10.1038/srep04215>.
- [46] X. Luo, Y. Zhao, J. Zhang, M. Toh, C. Kloc, Q. Xiong, S.Y. Quek, Effects of lower symmetry and dimensionality on Raman spectra in two-dimensional WSe₂, *Phys. Rev. B.* 88 (2013) 195313. <https://doi.org/10.1103/PhysRevB.88.195313>.
- [47] M. Staiger, R. Gillen, N. Scheuschner, O. Ochedowski, F. Kampmann, M. Schleberger, C. Thomsen, J. Maultzsch, Splitting of monolayer out-of-plane A₁' Raman mode in few-layer WS₂, *Phys. Rev. B.* 91 (2015) 195419. <https://doi.org/10.1103/PhysRevB.91.195419>.
- [48] P. Kumar, B. Singh, P. Kumar, V. Balakrishnan, Competing thermal expansion mismatch and lattice strain engineered growth of crack free WS₂ in-plane heterostructures, *J. Mater. Chem. C.* 6 (2018) 11407–11415. <https://doi.org/10.1039/C8TC04573A>.
- [49] T.G.A. Verhagen, K. Drogowska, M. Kalbac, J. Vejpravova, Temperature-induced strain and doping in monolayer and bilayer isotopically labeled graphene, *Phys. Rev. B.* 92 (2015) 125437. <https://doi.org/10.1103/PhysRevB.92.125437>.
- [50] T. Peña, S.A. Chowdhury, A. Azizimanesh, A. Sewaket, H. Askari, S.M. Wu, Strain engineering 2D MoS₂ with thin film stress capping layers, *2D Mater.* 8 (2021) 045001. <https://doi.org/10.1088/2053-1583/ac08f2>.
- [51] J.T. Mlack, P. Masih Das, G. Danda, Y.-C. Chou, C.H. Naylor, Z. Lin, N.P. López, T. Zhang, M. Terrones, A.T.C. Johnson, M. Drndić, Transfer of monolayer TMD WS₂ and Raman study of substrate effects, *Sci Rep.* 7 (2017) 43037. <https://doi.org/10.1038/srep43037>.
- [52] W.H. Chae, J.D. Cain, E.D. Hanson, A.A. Murthy, V.P. Dravid, Substrate-induced strain and charge doping in CVD-grown monolayer MoS₂, *Appl. Phys. Lett.* 111 (2017) 143106. <https://doi.org/10.1063/1.4998284>.

- [53] A. Michail, N. Delikoukos, J. Parthenios, C. Galiotis, K. Papagelis, Optical detection of strain and doping inhomogeneities in single layer MoS₂, *Appl. Phys. Lett.* 108 (2016) 173102. <https://doi.org/10.1063/1.4948357>.
- [54] F. Wang, I.A. Kinloch, D. Wolverson, R. Tenne, A. Zak, E. O'Connell, U. Bangert, R.J. Young, Strain-induced phonon shifts in tungsten disulfide nanoplatelets and nanotubes, *2D Mater.* 4 (2016) 015007. <https://doi.org/10.1088/2053-1583/4/1/015007>.
- [55] M.W. Iqbal, K. Shahzad, G. Hussain, M.K. Arshad, R. Akbar, S. Azam, S. Aftab, T. Alharbi, A. Majid, Gate dependent phonon shift in tungsten disulfide (WS₂) field effect transistor, *Mater. Res. Express.* 6 (2019) 115909. <https://doi.org/10.1088/2053-1591/ab485a>.
- [56] L. Paulatto, F. Mauri, M. Lazzeri, Anharmonic properties from a generalized third-order ab initio approach: Theory and applications to graphite and graphene, *Phys. Rev. B.* 87 (2013) 214303. <https://doi.org/10.1103/PhysRevB.87.214303>.
- [57] M. Lazzeri, S. Piscanec, F. Mauri, A.C. Ferrari, J. Robertson, Phonon linewidths and electron-phonon coupling in graphite and nanotubes, *Phys. Rev. B.* 73 (2006) 155426. <https://doi.org/10.1103/PhysRevB.73.155426>.
- [58] A. Matthäus, A. Ennaoui, S. Fiechter, S. Tiefenbacher, T. Kiesewetter, K. Diesner, I. Sieber, W. Jaegermann, T. Tsirlina, R. Tenne, Highly Textured Films of Layered Metal Disulfide 2H-WS₂ : Preparation and Optoelectronic Properties, *J. Electrochem. Soc.* 144 (1997) 1013. <https://doi.org/10.1149/1.1837522>.
- [59] L.-F. Huang, Z. Zeng, Roles of Mass, Structure, and Bond Strength in the Phonon Properties and Lattice Anharmonicity of Single-Layer Mo and W Dichalcogenides, *J. Phys. Chem. C.* 119 (2015) 18779–18789. <https://doi.org/10.1021/acs.jpcc.5b04669>.
- [60] Z.-Y. Wang, Y.-L. Zhou, X.-Q. Wang, F. Wang, Q. Sun, Z.-X. Guo, Y. Jia, Effects of in-plane stiffness and charge transfer on thermal expansion of monolayer transition metal dichalcogenide, *Chinese Phys. B.* 24 (2015) 026501. <https://doi.org/10.1088/1674-1056/24/2/026501>.
- [61] S.H. El-Mahalawy, B.L. Evans, The thermal expansion of 2H-MoS₂, 2H-MoSe₂ and 2H-WSe₂ between 20 and 800°C, *J Appl Cryst.* 9 (1976) 403–406. <https://doi.org/10.1107/S0021889876011709>.
- [62] Y. Ding, B. Xiao, Thermal expansion tensors, Grüneisen parameters and phonon velocities of bulk MT₂ (M = W and Mo; T = S and Se) from first principles calculations, *RSC Advances.* 5 (2015) 18391–18400. <https://doi.org/10.1039/C4RA16966B>.
- [63] A.G. Vieira, C. Luz-Lima, G.S. Pinheiro, Z. Lin, J.A. Rodríguez-Manzo, N. Perea-López, A.L. Elías, M. Drndić, M. Terrones, H. Terrones, B.C. Viana, Temperature- and power-dependent phonon properties of suspended continuous WS₂ monolayer films, *Vibrational Spectroscopy.* 86 (2016) 270–276. <https://doi.org/10.1016/j.vibspec.2016.08.004>.
- [64] L. Su, Y. Zhang, Y. Yu, L. Cao, Dependence of coupling of quasi 2-D MoS₂ with substrates on substrate types, probed by temperature dependent Raman scattering, *Nanoscale.* 6 (2014) 4920–4927. <https://doi.org/10.1039/C3NR06462J>.
- [65] E. Artacho, E. Anglada, O. Diéguez, J.D. Gale, A. García, J. Junquera, R.M. Martin, P. Ordejón, J.M. Pruneda, D. Sánchez-Portal, J.M. Soler, The SIESTA method; developments and applicability, *J. Phys.: Condens. Matter.* 20 (2008) 064208. <https://doi.org/10.1088/0953-8984/20/6/064208>.
- [66] J.M. Soler, E. Artacho, J.D. Gale, A. García, J. Junquera, P. Ordejón, D. Sánchez-Portal, The SIESTA method for ab initio order-N materials simulation, *J. Phys.: Condens. Matter.* 14 (2002) 2745–2779. <https://doi.org/10.1088/0953-8984/14/11/302>.
- [67] J.P. Perdew, Y. Wang, Accurate and simple analytic representation of the electron-gas correlation energy, *Phys. Rev. B.* 45 (1992) 13244–13249. <https://doi.org/10.1103/PhysRevB.45.13244>.
- [68] M.J. van Setten, M. Giantomassi, E. Bousquet, M.J. Verstraete, D.R. Hamann, X. Gonze, G.-M. Rignanese, The PseudoDojo: Training and grading a 85 element optimized norm-conserving

- pseudopotential table, *Computer Physics Communications*. 226 (2018) 39–54.
<https://doi.org/10.1016/j.cpc.2018.01.012>.
- [69] D.R. Hamann, Optimized norm-conserving Vanderbilt pseudopotentials, *Phys. Rev. B*. 88 (2013) 085117. <https://doi.org/10.1103/PhysRevB.88.085117>.
- [70] A. García, M.J. Verstraete, Y. Pouillon, J. Junquera, The psml format and library for norm-conserving pseudopotential data curation and interoperability, *Computer Physics Communications*. 227 (2018) 51–71. <https://doi.org/10.1016/j.cpc.2018.02.011>.
- [71] G. Lang, K. Karch, M. Schmitt, P. Pavone, A.P. Mayer, R.K. Wehner, D. Strauch, Anharmonic line shift and linewidth of the Raman mode in covalent semiconductors, *Phys. Rev. B*. 59 (1999) 6182–6188. <https://doi.org/10.1103/PhysRevB.59.6182>.
- [72] A.H. MacDonald, S.H. Vosko, P.T. Coleridge, Extensions of the tetrahedron method for evaluating spectral properties of solids, *J. Phys. C: Solid State Phys.* 12 (1979) 2991–3002.
<https://doi.org/10.1088/0022-3719/12/15/008>.
- [73] F. Liu, W. Wu, Y. Bai, S.H. Chae, Q. Li, J. Wang, J. Hone, X.-Y. Zhu, Disassembling 2D van der Waals crystals into macroscopic monolayers and reassembling into artificial lattices, *Science*. 367 (2020) 903–906. <https://doi.org/10.1126/science.aba1416>.
- [74] K. Momma, F. Izumi, VESTA 3 for three-dimensional visualization of crystal, volumetric and morphology data, *J Appl Cryst.* 44 (2011) 1272–1276.
<https://doi.org/10.1107/S0021889811038970>.